Sedimentary Geology 313 (2014) 1–14

Contents lists available at ScienceDirect

Sedimentary Geology

journal homepage: www.elsevier.com/locate/sedgeo

Application of attenuated total reflectance Fourier transform infrared spectroscopy in the mineralogical study of a landslide area, Hungary

Beatrix Udvardi [a, b], István János Kovács [b,*], Péter Kónya [b], Mária Földvári [b], Judit Füri [b], Ferenc Budai [b], György Falus [b], Tamás Fancsik [b], Csaba Szabó [a], Zoltán Szalai [c], Judith Mihály [d]

[a] Lithosphere Fluid Research Lab, Institute of Geography and Earth Sciences, Eötvös University, 1117 Budapest, Pázmány Péter sétány 1/c, Hungary
[b] Geochemical and Laboratory Department, Geological and Geophysical Institute of Hungary, 1143 Budapest, Stefánia út 14, Hungary
[c] Department of Environmental and Landscape Geography (Institute of Geography and Earth Sciences, Faculty of Science), Eötvös University, 1117 Budapest, Pázmány Péter sétány 1/c, Hungary
[d] Institute of Materials and Environmental Chemistry, Research Centre for Natural Sciences, Hungarian Academy of Sciences, 1117 Budapest, Magyar Tudósok Körútja 2, Hungary

ARTICLE INFO

Article history:
Received 19 May 2014
Received in revised form 27 August 2014
Accepted 28 August 2014
Available online 6 September 2014

Editor: J. Knight

Keywords:
ATR FTIR
Sediments
Landslide
Grain size
Anisotropy of calcite

ABSTRACT

This study demonstrates that the unpolarized attenuated total reflectance Fourier transform infrared spectroscopy (ATR FTIR) is a practical and quick tool to distinguish different types of sediments in landslide-affected areas, and potentially other types of physical environments too. Identification and quantification of minerals by ATR FTIR is implemented on a set of powdered natural sediments from a loess landslide (Kulcs, Hungary). A protocol including sample preparation, analytical conditions and evaluation of sediment ATR spectra is outlined in order to identify and estimate major minerals in sediments. The comparison of the defined FTIR parameters against qualitative and quantitative results of X-ray diffraction and thermal analysis was used to validate the use of ATR FTIR spectroscopy for the considered sediments. The infrared band areas and their ratios (water/carbonates; silicates/carbonates; kaolinite) appear to be the most sensitive parameters to identify strongly weathered sediments such as paleosols and red clays which most likely facilitate sliding and could form sliding zones. The effect of grain size and orientation of anisotropic minerals on the wave number and intensity of some major absorption bands is also discussed.

1. Introduction

1.1. Key minerals in landslides

Various techniques have been developed to classify minerals and monitor compositional changes of sediments. Currently, several complex and sometimes expensive analytical techniques are utilized for the mineralogical analysis of sediments (i.e., X-ray Fluorescence, Scanning Electron Microscope, Raman spectroscopy). Most of these methods require special sample preparation and considerable analysis and evaluation time. One of the alternative and supplementary methods for mineral analysis in sediments is infrared spectroscopy. The infrared spectra of sediments can be recorded using different infrared techniques such as transmission infrared (TIR), diffuse reflectance infrared Fourier transform (DRIFT) and attenuated total reflectance Fourier transform infrared (ATR FTIR) spectroscopy. Several studies have presented geological applications of ATR FTIR for qualitative phase identification in sediments and cements (e.g., Herbert et al., 1992; Hughes et al., 1995; Besson and Drits, 1997; Vaculíková and Plevová, 2005; Kumar and Rajkumar, 2013). Jian et al. (2009) identified smectite-rich sediments in the Anlesi landslide (China) based on TIR spectra, which demonstrated first the potential feasibility of infrared techniques in the identification of sliding zones. This is because infrared techniques are sensitive for identifying water-bearing (hereafter the term water includes both OH^- and H_2O species) minerals such as clay minerals and other sheet silicates (muscovite, illite, smectite, kaolinite, chlorite etc.). Weathered sediments usually contain these water-bearing minerals the proportions of which are indicative of the extent of weathering (Essington, 2004).

For geological studies, especially for landslides and slope failures, mineralogical investigation of sediments is essential. This is because a large abundance of sheet silicates (especially smectite) in slip zones is one of the fundamental controlling factors of sliding processes within landslides due to their high specific surface, water absorbing capacity and preferred orientation (Summa et al., 2010; Wang et al., 2011).

Smectite is the most important clay mineral group in terms of geotechnical behavior because of its swelling property, in contrast to kaolinite and micas (such as muscovite and illite). Consequently, smectite plays the dominant role in slope failures as recently demonstrated by Azañón et al. (2010).

Weathered sediments usually contain kaolinite as an indicator of advanced weathering. Kaolinite has typically platy morphology and

* Corresponding author. Tel.: +36 1 251 0999x381.
E-mail address: kovacs.istvan.janos@mfgi.hu (I.J. Kovács).

http://dx.doi.org/10.1016/j.sedgeo.2014.08.005
0037-0738/

commonly shows evidence for shear deformation. Thus the presence of kaolinite in slip zones and zones of discontinuity in clayey silty lithological formations can also facilitate slope failure due to its micromorphology (Summa et al., 2010). The accurate identification and quantification of kaolinite by X-ray diffraction (XRD), however, could be difficult when it coexists with other clay minerals. This is especially challenging when kaolinite is present in small quantities, namely less than about 10% of the sample. This is because the characteristic X-ray diffraction peaks of kaolinite overlap with those of chlorite at ~7 Å and ~3.5 Å. Especially in mixtures, kaolinite can therefore be overlooked in XRD traces (Guo and Underwood, 2011). Accuracy improves if the analytical methods include calibration with standards; however, those kinds of approaches are too long to be practical for a large number of samples (Środoń et al., 2001). Infrared spectroscopy techniques may be more sensitive to relatively low concentrations of kaolinite due to its intense OH^- vibrations between 3600–3700 cm^{-1} (Kodama and Oinuma, 1962).

Generally, slip zones develop along pre-existing zones of weakness which contain larger amounts of sheet silicates (especially smectite and kaolinite) and lower amount of carbonates. In addition, water–mineral interactions such as hydrolysis, argillation and dissolution of carbonates can contribute to slidings along pre-existing weak zones (Wen and Chen, 2007). Hence, it is important to study the variation of sheet silicate and carbonate contents in landslide-affected sediments for the purpose of detecting pre-failure indicators.

1.2. Analytical overview

Recent geological studies deal with the estimation of mineralogical composition in synthetic and natural mixtures of minerals with the application of IR techniques using for example multivariate statistical techniques (e.g., Breen et al., 2008; Adamu, 2010). However, classical methods such as X-ray powder diffraction are superior to infrared spectroscopy when mixtures contain more than 3 phases (Hillier et al., 2000). This is because the infrared spectra of sediments are usually characterized by numerous, very often overlapping, absorption bands. In addition, absorption bands are usually anisotropic; therefore their intensity is also dependent on the direction of the incident light with respect to the absorption indicatrix (Libowitzky and Rossman, 1996; Kovács et al., 2008; Sambridge et al., 2008). Furthermore, reproducibility of TIR and DRIFT measurements may be challenging. TIR requires the preparation of KBr pellets, which procedure involves pressing and grinding of the sample powder (i.e., mechanical effect, preferred orientation etc.), and chemical alterations may occur in contact with the KBr buffer (hydration, ion-exchange etc.). These mechanical and chemical effects along with scattering of infrared light at KBr–mineral interfaces may cause disturbances in the measured infrared spectrum (Dent, 1996).

DRIFT measurements are usually done in the near infrared region and the method has its limitations in the mid infrared region (i.e., when the wavelength is below 1200 cm^{-1}) due to interference effects created by particle size. Most of these effects could be reduced if the sample powder is mixed with KBr. However, to get optimal spectral quality, the degree of dilution of the sample powder with KBr may be different for each sample. A critical comparison of these infrared techniques can be found in Madejová (2003).

Compared to ATR FTIR spectroscopy, TIR and DRIFT methods still require relatively long sample preparation. However, ATR FTIR spectroscopy only requires finely ground and homogenized sample powder to obtain a representative spectrum. With the ATR FTIR technique it is also possible to study both wet suspensions and dry powders.

ATR FTIR has been used extensively in the study of polymers and organics (Planinsek et al., 2006; Urbaniak–Domagala, 2012) but its use is still relatively restricted in geological applications (Bertaux et al., 1998; Johnston and Premachandra, 2001; Reig et al., 2002; Guiliano et al., 2007), especially in qualitative phase identification. The intensity of characteristic absorption bands is usually related to the concentrations of the absorbing specie, through the Beer-Lambert law. Therefore recently a few studies have attempted the quantitative application of ATR FTIR for economically important sediments (e.g., Adamu, 2010; Palayangoda and Nguyen, 2012; Washburn and Birdwell, 2013).

There are several advantages of ATR FTIR in quantitative analysis. According to Glotch et al. (2007) the ATR technique does not suffer from the multiple scattering effects due to fine sample particle size that can make the interpretation of reflectance or emissivity spectra difficult. In fact, ATR is an ideal technique to identify minerals in fine grained (<10 μm) sediments because fine particles provide the best contact between the sample and the ATR element. Theoretically, proportionality between concentration of particular mineral constituents and their corresponding absorption bands is expected only if the mineral grains are similar sized, fully homogenized and are unoriented. Chemtob et al. (2010) revealed that absorbance is strongly grain size dependent where intensity increases with decreasing grain size. Therefore, the preparation of samples with small and homogeneous grain size is a key factor for more accurate quantitative ATR FTIR analysis (Palayangoda and Nguyen, 2012).

The objectives of this study includes: (1) to identify characteristic infrared bands and band areas of diagnostic minerals by ATR FTIR in natural slip-prone sediments; (2) to compare the variation of infrared band areas against estimated mineral compositions by X-ray powder diffraction (XRD) and thermal analysis (TA), and (3) to explain some typical particularities of the defined ATR FTIR parameters observed for clay minerals and carbonates which may be attributed to grain size and orientation effects, respectively.

The study illustrates the usefulness of the ATR FTIR technique for the discrimination of different sediment types with various clay and carbonate content. It is demonstrated that ATR FTIR spectroscopy could be a very effective tool for the identification of weakness zones in sediments which are typically characterized by high clay mineral (especially smectite and kaolinite) and low carbonate contents.

2. Study site

The Kulcs area is one of the largest active landslide affected areas in Hungary that is situated on the high bluff (high and steep bank) along the River Danube. The high bluff is 50–70 m above the average water level of the River Danube, and shows a steeper upper slope (about 30°) and a less steep lower slope (<10°) towards the river (Rónai et al., 1965).

Mass movements are reported from an approximately 1800 m long section of the river bank. The estimated total volume of landslides is 7.55×10^5 m^3, but four distinctive landslides were identified in 2011 with different slipped volume (Farkas, 2011).

The study area is covered by Neogene-Quaternary unconsolidated sediments. The basement formations consists of Miocene (Upper Pannonian) clayey and sandy sequences those are below 150–200 m in the background of the high bluff and outcrop in the river bed due to the morphology of the area and Quaternary tectonic movements (Rónai et al., 1965). This deposit is overlain by Pleistocene Old Loess Series including sand and brown to red paleosol zones in variable thicknesses. It is about 20–50 m in the high bluff and thins toward the river (typically less than 10 m thick). The old paleosol layers are characterized by clay-rich forest or subtropical soils (Pécsi and Schweitzer, 1993; Varga et al., 2011). The Young Loess Series is missing due to erosion. The cover deposits are soaked by rainfalls, floods and ground water flows to the River Danube and by highly pressurized water through the Upper Pannonian sand (Rónai et al., 1965).

The climate of the studied area is continental with a mean annual temperature of 9–10 °C. The mean annual precipitation is around 550–600 mm and concentrated in the late spring to summer (from May to July), as well as during late autumn (Szalai et al., 2005).

3. Materials and methods

3.1. Sample collection and preparation

Samples were taken from the southern landslide (roughly 10 m thick in average, area of 2.1×10^4 m^2, estimated volume of 15–450 $\times$ 10^3 m^3), where the slip zone is exposed along the riverbank (Farkas, 2011). Shallow boreholes (3–7 m) were drilled on the riverbank in a previously identified sliding zone (Farkas, 2011). Four distinct sediment units were identified macroscopically in the slipped body, from the top to the bottom as follows: 1) grey fluvial sediment, 2) yellow loess with intercalated yellow-light brownish paleosols, 3) red clay, and 4) yellow-grey sand–sandstone intercalated with yellow loamy units (Supplementary Fig. 1).

In this study, 43 sediment samples were collected from continuous core sections at various depths (Table 1). Only loamy units (referred to as loam hereafter) are considered from the yellow-grey sand–sandstone unit as the investigation of sand-sandstones with the applied infrared technique would not provide extra information for our purposes. The samples were mostly selected from the top and the bottom part of the particular units. The samples were numbered from top to bottom (for the exact sampling points see Supplementary Fig. 1).

Initial batch of 5 g was usually sieved from each sample below 63 μm, and further grinding was applied if it was necessary. The samples were homogenized by grinding in a porcelain mortar. In addition, we examine the effect of orientation on carbonate absorption bands in powder mixtures of sediments. For this study a cuboid (1.5 $\times$ 1.2 $\times$ 0.9 cm) was cut, ground and polished from a single idiomorphic and clean rombohedral calcite crystal with one pair of surfaces perpendicular to the c-axis of the crystal. The principal c-axis was identified based on the morphology of the original calcite crystal. Each pair of nominally parallel surfaces of the cuboid is almost perfectly parallel and was polished carefully to avoid any unwanted scattering effect. Then, the polished slabs of the calcite cuboid were placed onto the ATR plate and were measured by ATR FTIR.

Furthermore, four mechanical mixtures with different proportions of kaolinite (KGa-1, Georgia, USA) and calcite (Beremend, Hungary) were prepared. The binary mixtures were mixed with varying mass proportions of kaolinite and calcite as follows: 40.0, 59.8, 79.8, 90.0% kaolinite and 60.0, 40.2, 20.2, 10.0% calcite in the mixtures, respectively. A mass of 100 mg was prepared from each mixture.

3.2. Laser particle size distribution analysis

The particle size distribution was measured by the laser diffraction method using a Horiba Partica LA-950 V2 instrument, which measures particle sizes in a range from 0.01 μm to 3.0 mm. The samples were air dried, disaggregated and subsequently 1 g was treated with sodium pyrophosphate solution (50 g/l) overnight. Five minutes of ultrasonic treatment was applied to complete dispersion. Three repeated measurements of each sample were taken in order to monitor homogeneity of grain size distribution. In the calculation of particle size, the refractive index and the imaginary part were assumed to be 1.53 and 0.01, respectively (Jonasz, 1991; Eshel et al., 2004; Ozer et al., 2010). Among the three repeated measurements, the distribution was used which shows the best fit between the measured and theoretical distributions (Horiba, 2008). Grain size distribution of samples based on the USDA (United States Department of Agriculture) texture classification using the percentage of sand (2000–50 μm), silt (50–2 μm) and clay (<2 μm) was calculated. The proportion of grains below 500 nm was also determined.

3.3. ATR FTIR analysis

A similar volume of each sample (3–5 mg) was placed in polished glass containers and heated for at least 30 min at 80 °C in an oven immediately prior to the ATR FTIR measurements. After heating, the glass containers were closed and sealed with glass lids and parafilms, respectively. This heat treatment is thought to remove the majority of the absorbed water that substantially affects the vibrational modes of both the structural OH groups and H_2O molecules and prevents the aggregation of grains (Udvardi et al., 2012). The relatively low temperature of the heat treatment guarantees that it causes no first order alterations in the clay minerals' structure but facilitates significantly interpretation of the ATR spectra (see Tóth et al., 2012, for more details).

The sediment samples were studied by a Fourier-transform infrared spectrometer (Varian Model 2000) with a single pass ATR cell (Specac GoldenGate diamond ATR) and an MCT detector was used to obtain ATR spectra in the mid-infrared spectral range (400–4000 cm^{-1}). It

Table 1
List of samples from fluvial sediment, loess, paleosol, loam and red clay, and their granulometrical composition (%). Samples are collected from boreholes and marked with borehole ID (K1-6) and a number with increasing depth (B-No). The proportion of smallest grains of the clay fraction below 500 nm is also illustrated.

Sample type	Sample B-No	Sampling depth	Sand 50–2000 μm	Clay <2 μm	Silt 2–50 μm	<500 nm
		(m)	(%)	(%)	(%)	(%)
fluvial	K1-1	0.21–0.25	23.46	5.33	71.22	
sediment	K2-1	0.50–0.53	14.21	18.57	67.22	13.20
	K2-2	0.73–0.76	19.16	9.58	71.26	1.01
	K3-1	0.78–0.82	27.69	8.37	63.94	0.58
	K3-2	0.83–0.88	40.94	4.44	54.62	
	K3-4	1.08–1.12	18.39	4.81	76.80	0.11
	K4-1	0.55–0.60	38.62	5.92	55.47	
	K4-2	0.94–0.98	2.92	20.11	76.97	14.52
	K5-1	1.34–1.37	16.30	8.29	75.41	0.65
	K6-1	0.52–0.58	19.06	8.50	72.44	0.79
	K6-2	0.81–0.84	18.35	6.40	75.25	
	K6-3	1.08–1.11	17.66	11.48	70.86	4.25
	K6-4	1.29–1.34	23.27	8.46	68.27	0.57
Average			21.54	9.25	69.21	3.96
σ			9.95	4.92	7.35	5.75
loess	K1-2	0.77–0.80	3.94	7.37	88.69	0.53
	K2-3	1.69–1.73	15.65	20.42	63.94	14.29
	K2-4	2.12–2.15	17.54	19.41	63.05	12.22
	K2-5	2.52–2.55	20.99	12.89	66.12	7.96
	K2-7	2.82–2.87	0.15	7.21	92.64	1.59
	K3-9	2.26–2.29	17.40	4.83	77.78	0.10
	K3-10	2.77–2.80	17.58	5.60	76.82	0.11
	K3-12	3.58–3.61	23.10	5.38	71.53	0.15
	K3-13	3.71–3.74	4.71	12.59	82.70	8.28
	K4-3	1.31–1.35	0.43	12.65	86.93	9.23
	K4-7	2.78–2.88	10.19	12.29	77.52	5.08
	K4-8	3.42–3.46	13.42	11.63	74.96	7.07
	K5-3	2.50–2.54	22.91	4.56	72.53	
	K5-4	2.62–2.66	2.91	4.79	92.30	0.25
	K5-5	2.87–2.91	3.82	5.64	90.54	0.40
	K6-5	1.37–1.40	29.97	4.90	65.13	
Average			12.79	9.51	77.70	4.80
σ			9.26	5.21	10.33	5.01
loam	K1-3	1.84–1.88	24.45	3.89	71.66	
	K3-14	3.78–3.81	19.13	15.27	65.61	10.83
	K5-6	4.10–4.20	4.63	7.95	87.42	1.71
	K6-7	2.64–2.67	15.40	3.42	81.18	
	K6-8	3.52–3.56	3.78	6.72	89.50	1.50
Average			13.48	7.45	79.07	4.68
σ			9.06	4.77	10.24	5.33
paleosols	K2-6	2.64–2.68	20.89	8.95	70.17	1.10
	K3-5	1.26–1.30	20.20	4.81	74.99	0.12
	K3-6	1.57–1.62	19.52	5.95	74.53	0.14
	K3-7	2.03–2.07	21.26	5.42	73.32	0.10
	K3-8	2.15–2.17	21.61	6.05	72.35	0.11
	K3-11	3.39–3.43	18.88	6.36	74.76	0.30
Average			20.39	6.25	73.35	0.31
σ			1.05	1.43	1.86	0.39
red clay	K4-4	1.41–1.46	0.00	38.76	61.24	24.00
	K4-5	2.26–2.34	3.24	30.52	66.25	21.37
	K4-6	2.49–2.53	0.00	28.70	71.30	23.16
Average			1.08	32.66	66.26	22.85
σ			1.87	5.36	5.03	1.34

should be noted that each spectrum displays spectral features of the diamond ATR crystal between ~1800 and 2200 cm^{-1}. The number of scans and the spectral resolution were 128 and 4 cm^{-1}, respectively.

ATR FTIR measurements of binary mixtures and the calcite cuboid were performed using a Bruker Vertex 70 spectrometer equipped with a diamond Bruker Platinum ATR accessory and an MCT detector. The number of scans and the spectral resolution were also 128 and 4 cm^{-1}. One of the parallel slabs of the calcite cuboid was placed onto the ATR plate in two perpendicular and one diagonal positions by rotating the cuboid. In the anisotropic sections the absorbance characteristics changes with the direction of the incident light upon rotation.

The sample powders are pressed with constant pressure (70 Ncm) on a small crystal plate (3×3 mm) which allows for reproducible spectra obtained from different batches. The fact that specimens usually have limited contact with the air, and the sample layer is thicker than the penetration depth of infrared light (d_p) is reflected in the high reproducibility of the infrared spectra. However, water gain sometimes occurred during repeated analysis of the consecutive proportions of the same sample batch. This water gain was especially profound in clay rich sediments. Consequently, the first spectrum of each sample batch is reported and used in further discussion because it is thought to be the least affected by the unwanted spectral contribution of atmospheric moisture (Tóth et al., 2012).

Baseline and ATR corrections were done by applying the Resolutions Pro software package. ATR correction is necessary to account for the wave number dependency of the penetration depth, which procedure make ATR spectra resembling more closely normal TIR spectra. Using the refractive indices of common minerals in sediments (Lide, 2005), the authors calculated the minimal and maximal depth of penetration at 1000 cm^{-1} ($d^{-1}_{p1000\ cm}$) and at 3400 cm^{-1} ($d^{-1}_{p3400\ cm}$) for common minerals in sediments (Table 2).

For the calcite cuboid, advanced ATR correction of the OPUS software was used. The incident angle is set to 45°, the number of reflections is 1 and the refractive index of the calcite is changed from 1.486 for anisotropic to 1.658 for isotropic sections. For the diagonal measurements in anisotropic sections the average of these two extreme indices is used for the advanced ATR correction.

The positions of the most intense bands in the sediment samples were measured by the peak-pick tool of the OPUS. Besides the 'peak picking' method for the identification of band positions which is optimal for sharper absorption bands, additional individual bands – as parts of broad and complex bands – are identified by the second derivative method of the OPUS 6.5 using a 9-point Savitzky–Golay filter to enhance the resolution of superimposed bands.

Infrared band areas (A, i.e. integrated intensities), containing all bands (overlapping bands and shoulders), were determined instead of linear intensities (band heights) for quantitative evaluation, as infrared band areas are thought to be less sensitive to the presence of other overlapping bands (Libowitzky and Rossman, 1997). The most commonly applied approach for the integration of bands is when the area between the line, connecting the intersections of the lower and upper limits of the integration, and the spectrum is considered. Following this routine the area under characteristic absorption bands are determined (Supplementary Tables 1, 2).

The infrared band area under a very wide range of absorbance conditions is linearly proportional to the concentration of the absorbing species. It is expected, therefore, that ATR absorbances are proportional to concentration, analogous to the way concentration is related to absorbance in TIR. It follows that there should be linear correlation between infrared band areas of characteristic minerals and their estimated modal abundance by XRD and TA. In strongly absorbing minerals and/or in highly anisotropic sections unpolarized absorbance may underestimate the real concentrations (Libowitzky and Rossman, 1996). Based on previous experiences, however, the large number of unoriented grains and the low linear absorbances (<0.3) make the application of the unpolarized ATR FTIR method feasible for quantitative purposes (Kovács et al., 2008; Sambridge et al., 2008).

Table 2
Minimum and maximum refractive indices of minerals (RI_{max}, RI_{min}; Lide, 2005) and their penetration depth (d_p) at 1000 cm^{-1} and 3400 cm^{-1}. $\Delta RI = RI_{max} - RI_{min}$.

Minerals	RI_{min}	RI_{max}	ΔRI	d_{pmin}	d_{pmax}	d_{pmin}	d_{pmax}
				at 1000 cm^{-1} (μm)		at 3400 cm^{-1} (μm)	
quartz	1.54	1.55	0.01	2.21	2.27	0.65	0.67
calcite	1.49	1.66	0.17	1.18	4.04	0.56	1.19
dolomite	1.50	1.68	0.18	1.97	5.57	0.58	1.64
chlorite	1.61	1.62	0.01	2.85	3.01	0.84	0.89
muscovite	1.56	1.60	0.04	2.34	2.74	0.69	0.81
illite	1.56	1.59	0.03	2.32	2.60	0.68	0.76
smectite	1.55	1.57	0.02	2.25	2.40	0.66	0.71
kaolinite	1.55	1.57	0.02	2.24	2.36	0.66	0.69

3.4. X-ray powder diffraction

The XRD analysis of whole-rock powder samples were carried out using a Phillips PW 1710 diffractometer with a Cu anode at 40 kV accelerating voltage and 30 mA tube current using graphite monocromator at a goniometer speed of 2°θ min^{-1} from 2 to 66° 2θ.

A semi-quantitative assessment of the relative concentrations of phases was performed by relative intensity ratios and full width at half maximum (FWHM) of specific reflections of minerals by using XDB Powder Diffraction Phase Analytical software 2.7 (Sajó, 1994). The full width at half maximum of 10 Å reflection ($FWHM_m$), representing micas (both muscovite and illite), was also measured. Mica can be classified as muscovite below the 0.30 value of $FWHM_m$ following a previous study that found that samples are more muscovitic below this value, and more illitic above it (Földvári and Kovács–Pálffy, 2002).

3.5. Thermal analysis

Thermal analysis were carried out by Derivatograph–PC from room temperature (20 °C) to 1000 °C (10 °C/minute) using Al_2O_3 as inert material. A total of 100 mg of samples was heated in a ceramic crucible. The quantitative determination of the thermally active minerals is based on stoichiometric calculations of decomposition processes of the identified minerals due to loss of mass during heating (Paulik and Paulik, 1981; Földvári, 2011). Loss of molecular water was also measured.

4. Results

4.1. Grain size distribution of different types of sediments

Measured grain sizes in samples vary in the range of 0.061–350 μm. The grey fluvial sediment contains on average the largest fraction of coarse grains (average 12.3%; min. 1.2–max. 25.6%) (Fig. 1, Table 1). Relatively low abundance of coarse grains was found only in the two grey fluvial sediment samples (1.2% for K4-2 and 7.3% for K2-1). Except for these two samples, grey fluvial sediment is silt loam with about 10% clay (Fig. 1). Loess shows higher variation in the amount of the coarse grain fraction than paleosols, loam and red clay. Based on the USDA texture classification triangle, loess, paleosols and two samples of loam (K3-14, K1-3) are silty loams. In addition four loess (K1-2, K4-3, K5-4, K5-5) and two loam (K5-6, K6-8) samples are silts with less than 5% sand. One sample of loam (K6-7) is silt with 15.4% sand. The most homogeneous granulometrical composition was found in paleosols, where the standard deviations of different grain size fractions are below 2%. Loess has a slightly higher percentage of clay particles than loam and paleosols. Two loess samples (K2-3, K2-4) have almost 20% clay (Fig. 1). The red clay is silty clay loam and contains more

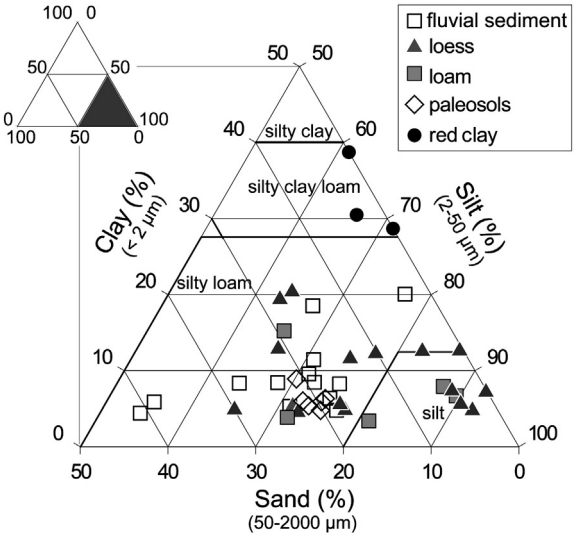

Fig. 1. USDA textural triangle shows the classification of sediments analyzed in this study.

than 28% clay, differing most considerably from grey fluvial sediment, loess, paleosol, and loam samples.

The amount of grains below 500 nm is variable: with an average at 2.7% in grey fluvial sediment, 4.2% in loess, 2.81% in loam, 0.3% in paleosols and 22.8% in red clay (Table 1). There are only two grey fluvial sediment (K2-1, K4-2) and loess samples (K2-3, K2-4) and one loam (K3-14) sample which contain greater than 10% grains below 500 nm.

4.2. Mineralogical compositions by different methods

4.2.1. ATR FTIR

The characteristic wave numbers (cm^{-1}) of the identified bands are observed in the range of 4000–400 cm^{-1} (see Table 3 for a comprehensive summary). Note, however, that band positions could be slightly or considerably shifted from reported band wave numbers obtained by both TIR and ATR techniques (Wada, 1967; Farmer, 1974; Van der Marel and Beutelspacher, 1976; Hlavay et al., 1978; Madejová and Komadel, 2001; Schroeder, 2002; Vaculíková and Plevová, 2005; Jung et al., 2010) due to the different infrared methods (i.e., TIR, DRIFT, ATR FTIR), sample preparation (pressed pellet or powder sample), changing chemistry of minerals (i.e., Mg incorporation in calcite; different cation occupancy in layers and interlayers of smectite etc.) and anisotropy of infrared absorption (in which certain indicatrix section(s) may become dominant during analysis).

Fig. 2 shows representative ATR spectra for the major sediment units (i.e., grey fluvial sediment, loess, loam, paleosols and red clay) with the band assignments for the most prominent absorption bands. The typical ATR spectra of grey fluvial sediment and loess display lower absolute absorbances than loam, paleosols and red clay. The band at 1428 ± 11 cm^{-1} in the ATR spectrum of grey fluvial sediment is broader than in other sediments and the presence of the band at 728 ± 2 cm^{-1}, representing dolomite, is better expressed. The carbonate band at 874 ± 2 cm^{-1} usually can be well resolved from the broad band of silicate minerals at 989 ± 8 cm^{-1} in the grey fluvial sediment and loess.

Paleosols and red clays display characteristic spectral features in that the band at 1428 ± 11 cm^{-1} has much lower absolute intensity relative to grey fluvial sediment, loess and loam, whereas the band at 1635 ± 1 cm^{-1} related to the bending of molecular water, mainly in smectite, shows higher absolute intensity (Fig. 2).

Significant shifts in wave numbers occur at 989 ± 8 cm^{-1} (referred to as $\nu_{silicates}$ hereafter) and at 1428 ± 11 cm^{-1} (referred to as $\nu_{carbonates}$ hereafter) in the ATR spectra of samples corresponding to Si-O and CO_3^{2-} vibrations, respectively (Table 3). The $\nu_{silicates}$ shows the highest average wave number in the grey fluvial sediment (996 ± 5 cm^{-1}) and decrease gradually from the loess (989 ± 7 cm^{-1}) to red clay (975 ± 1 cm^{-1}) through loam (985 ± 2 cm^{-1}), paleosols (984 ± 4 cm^{-1}). The $\nu_{carbonates}$ appears at slightly higher wave numbers in paleosols (1439 ± 10 cm^{-1}) in decreasing order red clay (1433 ± 1 cm^{-1}) loam (1433 ± 8 cm^{-1}) loess (1424 ± 14 cm^{-1}) grey fluvial sediment (1423 ± 7 cm^{-1}) and this particular wave number shows large variation in loess samples.

Based on the qualitative analysis of sediments' ATR FTIR spectra, characteristic infrared band areas are defined for main minerals or

Table 3
ATR FTIR observed wave numbers (cm^{-1}) of sediment samples with mineral identifications. Standard deviation of band positions (σ) among samples is reported.

wave numbers				Band assignments[1]	Minerals	References[2]
(cm^{-1})	σ[3]	A[4]	B[5]			
3696		sh	m	νOH, inner surface	kaolinite	1, 2, 3, 4, 5
3664		2nd		νOH, inner surface	kaolinite	1, 2, 3, 5
3645		2nd		νOH, inner surface	kaolinite	1, 2, 3, 5
3620			s	νOH	muscovite, illite, smectite, kaolinite	2, 3, 5
3557	6	sh	w	νOH	chlorite	2, 4, 6, 7
3402	7		s	νwater-OH	smectite, chlorite	4
2988			w	νC-H	organic material	6
2923			w	νC-H	organic material	6
2877			w	νC-H	organic material	6
2850		2nd		νC-H	organic material	6
1798			m	νCO_3	calcite, dolomite	2, 4
1635			m	δwater-OH	smectite	6
1428	11		s	νCO_3, asym	calcite, dolomite	2, 4, 6
1412	16	2nd		νCO_3, asym	calcite, dolomite	2, 4, 6
1396		2nd		νCO_3, asym	calcite, dolomite	2, 4, 6
1162		sh	m	νSi-O, asym	quartz	6
1117		2nd		νSi-O	kaolinite	2, 3
1089		2nd		νSi-O	kaolinite, quartz, chlorite	2, 4, 6
1060		2nd		νSi-O	illite, muscovite	2, 6
1030		2nd		νSi-O	muscovite, illite, kaolinite	4, 6
1002		2nd		νSi-O	smectite, kaolinite	3, 6
989	8		s	νSi-O	muscovite, illit, smectite, kaolinite	3, 6
977		2nd		νSi-O	chlorite	4, 6, 7
933		2nd		δAl-OH	kaolinite	2, 3
909		sh	m	δAl-Al-OH	muscovite, illite, smectite, kaolinite	3, 4
874		sh	s	δCO_3, out of plane	calcite, dolomite	2, 4, 6
847		2nd		δAl-Mg-OH	smectite	2, 3, 4
830			w	δAl-O	muscovite, illite	2, 4
796			s	νSi-O, sym	quartz	2, 4, 6
778			s	νSi-O, sym	quartz	2, 4, 6
759		2nd		δAl-O-Si	muscovite, illite	2, 4
748	12	2nd		δAl-Mg-OH, δAl-O-Si	muscovite, illite	2, 4
728			m	δCO_3, planar bending	dolomite	2, 6
713			m	δCO_3, planar bending	calcite	2, 4, 6
695			s	δSi-O, sym	quartz	2, 4
674		2nd		δAl-O-Si	chlorite	2, 6
649			m	δSi-O	smectite, chlorite	6
533			s	δAl-O-Si	muscovite, illite, smectite	2, 3
514		2nd		δSi-O	quartz	2, 6, 8

[1] ν: stretching mode, δ: bending mode, sym: symmetrical vibration, asym: asymmetrical vibration.
[2] Minerals are assigned using available data from literature as follows: 1) Wada, 1967; 2) Farmer, 1974; 3) Madejová and Komadel, 2001; 4) Vaculíková and Plevová, 2005; 5) Jung et al., 2010; 6) Van der Marel and Beutelspacher, 1976; 7) Schroeder, 2002; 8) Hlavay et al., 1978.
[3] Standard deviaton of band maximum is indicated only above the spectral resolution (4 cm^{-1}).
[4] sh: shoulder, 2nd: identified only on the second-derivative spectrum.
[5] Column B represents the intensity of bands; w: weak, m: medium, s: strong.

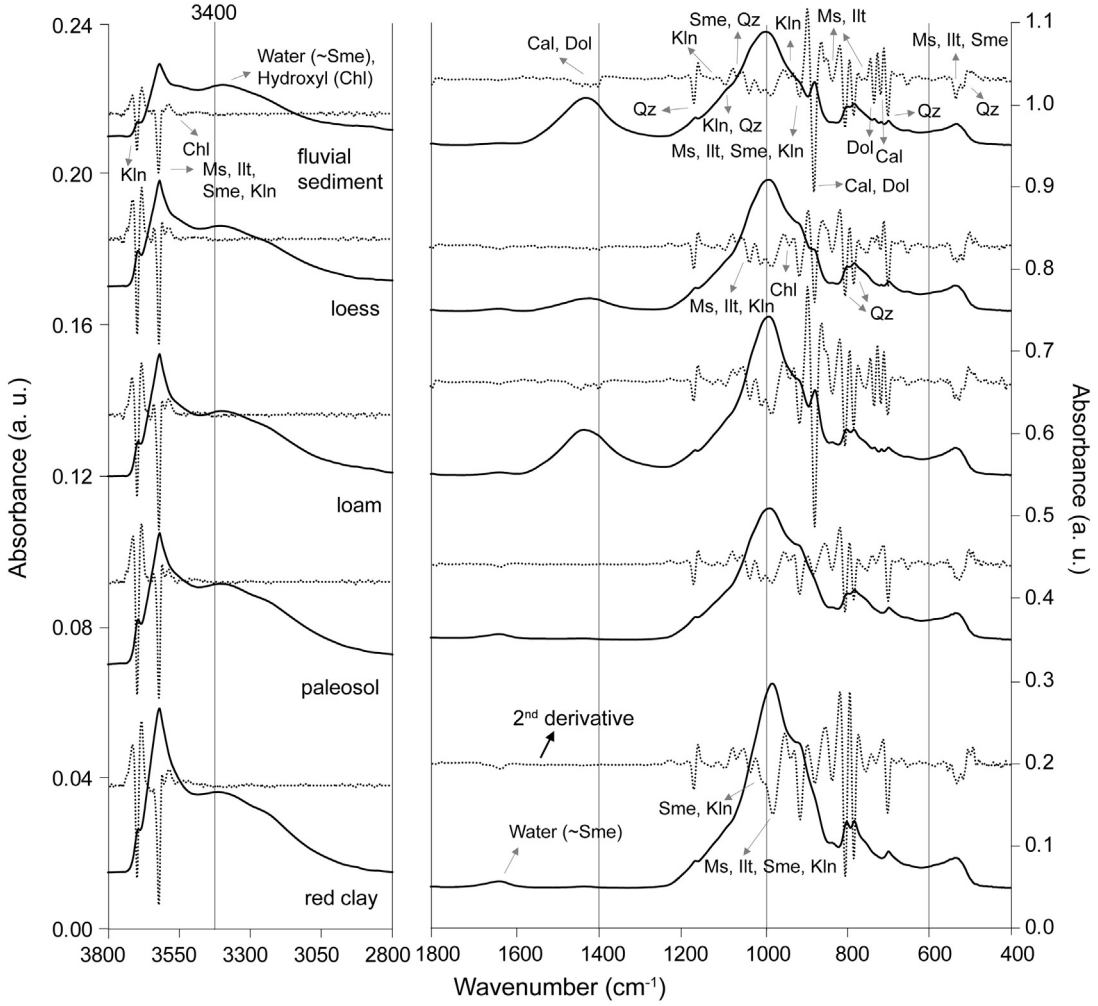

Fig. 2. Selected ATR FTIR spectra of the five sediment types with their generalized assignments marked. The underlying bands contributing to the baseline-corrected spectra were determined using the second derivative method (indicated by dotted line). Qz: quartz, Cal: calcite, Dol: dolomite, Chl: chlorite, Ms: muscovite, Ilt: illite, Sme: smectite, Kln: kaolinite.

group of minerals so as to facilitate quantitative evaluation. Sheet silicates such as muscovite ± illite, smectite, chlorite and kaolinite could be quantified by taking the area under the broad absorption band in the range 3000–3740 cm^{-1} (referred to as $A_{sheet\ silicates}$ hereafter) and 825–1235 cm^{-1} (referred to as $A_{silicates}$, see below for more detailed explanation). This latter area also includes the contributions of quartz and feldspar, however, as we shall demonstrate later this does not invalidate the use of this infrared band area for quantitative purposes. Integrated area of carbonates in the range 1235–1585 cm^{-1} (referred to as $A_{carbonates}$ hereafter) and at 874 ± 2 cm^{-1} (referred to as $A_{carbonates\text{-}2}$ hereafter) are considered for quantification. The latter band is evaluated individually in each sample by defining individual integration limits, given that it is difficult to define uniform integration limits for this band in all the samples. This is because the $A_{carbonates\text{-}2}$ (Fig. 2) appears as a shoulder on the broader and more intense band in the range of 825–1235 cm^{-1}. The $A_{carbonates\text{-}2}$, therefore, contributes to the area of the 825–1235 cm^{-1} band so that its subtraction from the area of the 825–1235 cm^{-1} leaves roughly the area of sheet silicates (referred to as $A_{silicates}$ hereafter). The infrared band areas are shown in Supplementary Tables 1 and 2.

The amount of molecular water is quantified by defining the integrated area in the range 1585–1725 cm^{-1} (referred to as A_{water} hereafter). The quantification of kaolinite is done by constraining the integrated area of the band at ~3697 cm^{-1} (referred to as $A_{kaolinite}$ hereafter). This latter band of kaolinite should also be evaluated individually by defining suitable integration limits for each sample, analogous to that applied for $A_{carbonates\text{-}2}$.

The minimum, maximum and average infrared band areas of these parameters in different types of sediments are plotted in Fig. 3. Infrared band areas show systematic variations in different sedimentary units, which may facilitate their identification based solely on their ATR FTIR spectra if other conventional methods are not available. The $A_{sheet\ silicates}$ shows an increasing tendency in the following sequence: grey fluvial sediment, loess, loam, red clay and paleosol (Fig. 3A). The highest variation between maximum and minimum infrared band areas is observed in the loess samples. A similar tendency is observed for the A_{water} but in this case the highest value is for the red clays instead of the paleosols (Fig. 3A). The difference between the maximum and minimum values for loess is nearly as high as for loam. The $A_{silicates}$ shows a similar trend to $A_{sheet\ silicates}$ and A_{water} and reaching the highest value in the red clay (Fig. 3A and B). $A_{carbonates\text{-}2}$ and $A_{carbonates}$ show an opposite trend to that of $A_{kaolinite}$, $A_{sheet\ silicates}$, A_{water} and $A_{silicates}$ as these decrease gradually from grey fluvial sediment to loess, loam, paleosols and red clay (Fig. 3C). The $A_{kaolinite}$ for red clay and paleosol is higher than for grey fluvial sediment, loess and loam (Fig. 3B).

4.2.2. X-ray powder diffraction

Result of whole rock samples' XRD analysis shows that variable amounts of quartz, carbonates (calcite > dolomite) and sheet silicates (muscovite ± illite > chlorite > smectite) are present in the samples;

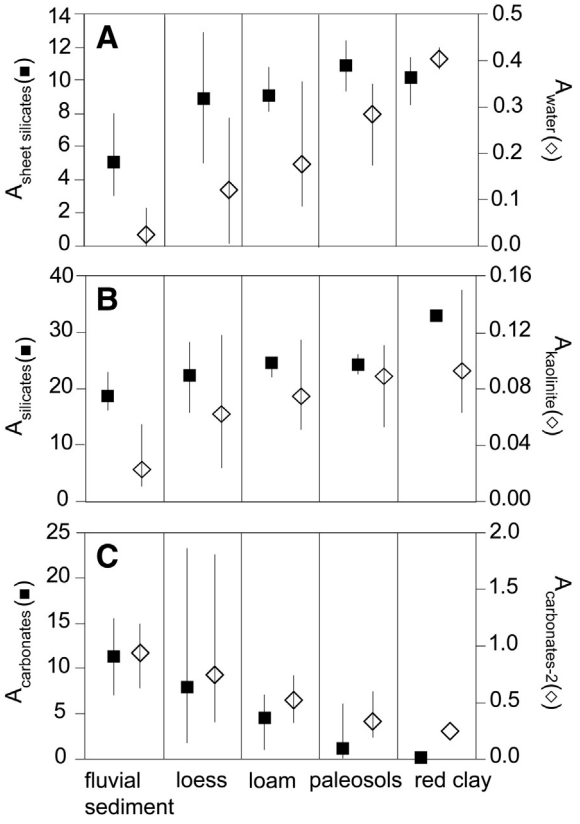

Fig. 3. Characteristic ranges for particular infrared band areas (indicated by the extent of lines) and their average values (indicated by diamonds and rectangles) are presented for the five sediment types. The ranges of infrared band areas are calculated from the infrared spectra of sediments (see Supplementary Table 2, for more details) as follows: A) A_{water} and $A_{sheet\ silicates}$, B) $A_{silicates}$ and $A_{kaolinite}$, C) $A_{carbonates}$ and $A_{carbonates\text{-}2}$.

feldspars (plagioclase (0–8%) > K–feldspar (1–3%)) and goethite (0–3%) appear in minor amounts (Supplementary Table 3). Samples contain only traces of kaolinite and gypsum as indicated by the low relative intensities of their diagnostic reflections. Percent amount of kaolinite is in some samples of loess (tr.—2%) and one sample of grey fluvial sediment (tr.—3%), and even amphibole (tr.—1%) and pyrite (1%) appear also sporadically. Low amount of amorphous phase is present as well, especially in paleosols (1–5%) and red clay (3%). One sample of paleosol contains 5% of amorphous phase (K3-11).

Averaged content of quartz is about 35%, except paleosol samples with 54% but varies in a broad range, especially in loess (17–57%) and in loam (26–61%).

The total amount of carbonates is higher in grey fluvial sediment (average 35%, 19–45%) than in paleosols (5%, 0–22%), in loam (22%, 7–31%) and red clay (1%, 0–2%), and even loess (27%, 9–50%) are more calcareous. In the grey fluvial sediment, dolomite (2–30%) is commonly more than calcite (12–39%) whereas loess and loam contain two or more times calcite than dolomite. Dolomite does not occur in the red clay. One red clay sample (K4-5) and two samples of paleosols (K2-6, K3-11) contain only calcite.

Content of sheet silicates also varies in a broad range. Compared with the abundance of sheet silicates in the sediments, red clay (59%, 53–68%), loam (34%, 22–39%) and paleosols (31%, 19–40%) contain a greater amount of sheet silicates than loess (30%, 19–47%) and grey fluvial sediment (25%, 17–33%).

Among sheet silicates, muscovite ± illite (14%, 8–16%), chlorite (9%, 5–12%), smectite (5%, 2–11%) are found in the grey fluvial sediment. A similar quantitative sequence of sheet silicates occurs also in loess, paleosols and loam. The average content of muscovite ± illite is 24% for red clay (24–25%), 16% loam (8–20%), 15% loess (8–22%), 14% paleosols (10–17%).

Full width at half maximum of muscovite ± illite ($FWHM_m$) varies between 0.22° and 0.45° and the average value is 0.30° in the samples. According to this value, the samples of red clay (0.43, 0.41–0.45) are illitic and even loess (0.30, 0.23–0.36), paleosols (0.35, 0.27–0.55) and grey fluvial sediment (0.28, 0.22–0.41) have higher values of $FWHM_m$. Paleosols (10%, 8–12%) and loam (12%, 8–14%) contain more chlorite than loess (9%, 6–16%) and red clay (8%, 5–12%). Estimated amount of smectite is 6% for loess (2–13%), 6% loam (5–8%), 9% paleosols (5–15%) and 32% red clay (22–37%).

4.2.3. Thermal analysis

Analysis of thermal curves indicates five characteristic temperature ranges that represent release of volatiles from minerals and their phase transitions. For all samples, the first step is loss of absorbed water between 47-268 °C (DTG curve minimum of 91 ± 8 °C) and loss of interlayer water from smectite between 137-364 °C (DTG curve minimum of 169 ± 16 °C) during heating. In the range of 313-792 °C (DTG curve minimum point: 530 ± 31 °C), the clay structures lose their water and carbonates structures start to disintegrate. At high temperature, between 573-962 °C (DTG curve minimum point: 819 ± 37 °C), carbonates decompose completely and oxides and silicate phases form. Supplementary Table 4 represents the estimated mineral composition of samples by TA. In a large number of samples, thermal dissociation of $CaCO_3$ and $MgCO_3$ from dolomite cannot be distinguished due to its weathered state (Földvári and Kovács-Pálffy, 2002). Thus the total content of dolomite + calcite was calculated.

The identified minerals in samples are muscovite ± illite, smectite, chlorite, calcite, dolomite and small amount of goethite and kaolinite. Among micas, hydromuscovite is also identified through its dehydroxylation temperature (620–650 °C) between muscovite (820–920 °C) and illite (~550 °C). Hydromuscovite is a hydrated form of muscovite containing little interlayer water from the replacement of K to H_3O^- (marked in parentheses, in the column of micas, Supplementary Table 4) (Földvári, 2011). It should be noted that the XRD pattern of hydromuscovite is very similar to muscovite, therefore, their identification is only possible the careful analysis of the thermal curves of samples. The thermal curve of hydromuscovite shows dehydroxylation at lower temperatures and contains a very small amount of interlayer water. In this study we considered hydromuscovite as illite. Traces of gypsum and organic material are also present. Pyrite occurs in one sample of grey fluvial sediment (K3-1).

According to TA, sheet silicates are abundant in samples of red clay (average 61%, min. 51–max. 68%), and even paleosols (23%, 16–30%) contain a larger percentage of sheet silicates compared to grey fluvial sediment (11%, 0–23%), loess (6–47%, 19%) and loam (17%, 14–24%).

Averaged content of smectite increases in the following sequence: 3% for grey fluvial sediment (1–6%), 6% loess (1–13%), 7% loam (4–15%), 10% paleosols (6–13%) and 23% red clay (21–26%). The total amount of micas (hydromuscovite and muscovite ± illite, $\Sigma_{ilt,\ mu,\ hym}$) is higher in red clay (25%, 24–26%) and in paleosols (13%, 10–15%) than in grey fluvial sediment (8%, 13–11%) and loess (13%, 2–22%). A similar tendency is found for chlorite; 7% grey fluvial sediment (0–12%), 9% loess (5–15%), 10% loam (8–13%), 10% paleosols (7–15%), 12% red clay (4–20%).

The amount of calcite is usually more than dolomite in sediments, and the total carbonate contents are 35% for grey fluvial sediment (23–43%), 26% loess (7–52%), 22% loam (8–28%), 4% paleosols (0–20%) and 1% red clay (0–2%). Red clay samples do not contain dolomite.

The mass change during loss of molecular water is summarized in Supplementary Table 4. It is higher in the red clay (average 3.77%, min. 3.39–max. 4.09%) and in the paleosols (1.61%, 1.22–2.04%) than in the grey fluvial sediment (0.28%, 0.03–0.91%), loess (1.05%, 0.14–2.16%) and loam (0.88%, 0.61–1.32%).

5. Discussion

5.1. Infrared features of minerals and their estimated content by XRD

The defined ATR FTIR parameters were first compared to the most common analytical technique for phase identification. Fig. 4A shows a closely linear relationship between sheet silicate content determined by XRD and $A_{sheet\ silicates}$ for the five types of sediments considered in this study. The plot indicates clustering of the different sediments. The grey fluvial sediment has a small amount of sheet silicates and low $A_{sheet\ silicates}$ values partly overlapping with the loess samples which show the most significant scattering in the plot. Loam and paleosol samples partially overlap with loess samples, however, paleosols are above, whereas most of the loam samples are below the trend line. The red clay comprises the most distinctive group which shows very high sheet silicate content at relatively low $A_{sheet\ silicate}$ value (therefore these samples fall off the linear trend defined by the other samples).

The sheet silicates vs. $A_{silicates}$ plot also reflects lower values for grey fluvial sediment overlapping with loess, loam and paleosol (Fig. 4B). The red clay and one loess (K4–8) samples occur at high sheet silicate content and $A_{silicates}$ values.

The illite and smectite ($\Sigma_{ilt,\ sme}$) content can absorb more water due to their relatively high surface, shows relatively good relationship with $A_{silicates}$ and $\nu_{silicates}$ (Fig. 5A and B). There is a positive correlation in the $\Sigma_{ilt,\ sme}$ vs. $A_{silicates}$ plot (Fig. 5A). On the other hand, there is an inverse correlation in the plot of $\Sigma_{ilt,\ sme}$ vs. $\nu_{silicates}$ (Fig. 5B). Loam samples fall below the trendline in $\Sigma_{ilt,\ sme}$ vs. $\nu_{silicates}$ plot. Red clay shows higher $\Sigma_{ilt,\ sme}$, $A_{silicates}$ and $\nu_{silicates}$, differing clearly from the other sediment types.

Among sheet silicates, the abundance of smectite appears to correlate positively with A_{water} (Fig. 6A). Paleosols and red clay have higher smectite content and A_{water} values than grey fluvial sediment, loess and loam. The calculated A_{water} is only about 0.01 in carbonate rich samples of grey fluvial sediment and loess.

Carbonate content (calcite and dolomite) by XRD vs. $A_{carbonates}$ and $\nu_{carbonates}$ are presented in Fig. 7A and B. The carbonate content shows a positive and negative correlation with $A_{carbonates}$ and $\nu_{carbonates}$, respectively. Red clay and paleosol samples form a rather distinct group characterized by low carbonate content and $A_{carbonates}$ values (Fig. 7A). Grey fluvial sediment has the highest carbonate content and $A_{carbonates}$ values. In addition, the carbonate band of grey fluvial sediment samples appears at the lowest wave number among all the sediment types. For the loess samples, all the parameters ($\nu_{carbonates}$, $A_{carbonates}$ and carbonate content) vary significantly overlapping with grey fluvial sediment and loam samples (Fig. 7A and B).

5.2. Infrared features of minerals and their estimated content by TA

The relations between infrared band areas and carbonate and mica content determined by TA are consistent with those determined by XRD measurements (Figs. 5, 7).

The sheet silicates content by TA vs. $A_{sheet\ silicates}$ plot is very similar to the sheet silicates by XRD vs. $A_{sheet\ silicates}$ (Fig. 4C and D). The abundances of smectite, illite and hydromuscovite ($\Sigma_{ilt,\ hym,\ sme}$) by TA show similar values to the estimated abundance of smectite and illite by XRD ($\Sigma_{ilt,\ sme}$). This is because it seems that the illite content defined by the XRD method (as >0.30) equals to the illite plus hydromuscovite content seen by the TA (Supplementary Tables 3, 4). The hydromuscovite is most probably seen as illite by the XRD. Note, however, that TA can resolve the peak temperatures related to the hydroxyl and water loss of illite and hydromuscovite. Thus, no wonder that both $\Sigma_{ilt,\ hym,\ sme}$ and $\Sigma_{ilt,\ sme}$ correlate with $A_{silicates}$ and $\nu_{silicates}$ (Fig. 5A–D).

Fig. 6B shows the correlation between smectite contents by TA and A_{water} values, which resemble very closely the smectite content by XRD and A_{water} plot (Fig. 6A).

Carbonate content by TA vs. $A_{carbonates}$ and $\nu_{carbonates}$ plots are presented in Fig. 7C and D, which are almost identical to the trends defined by XRD determined carbonate contents (Fig. 7A and B).

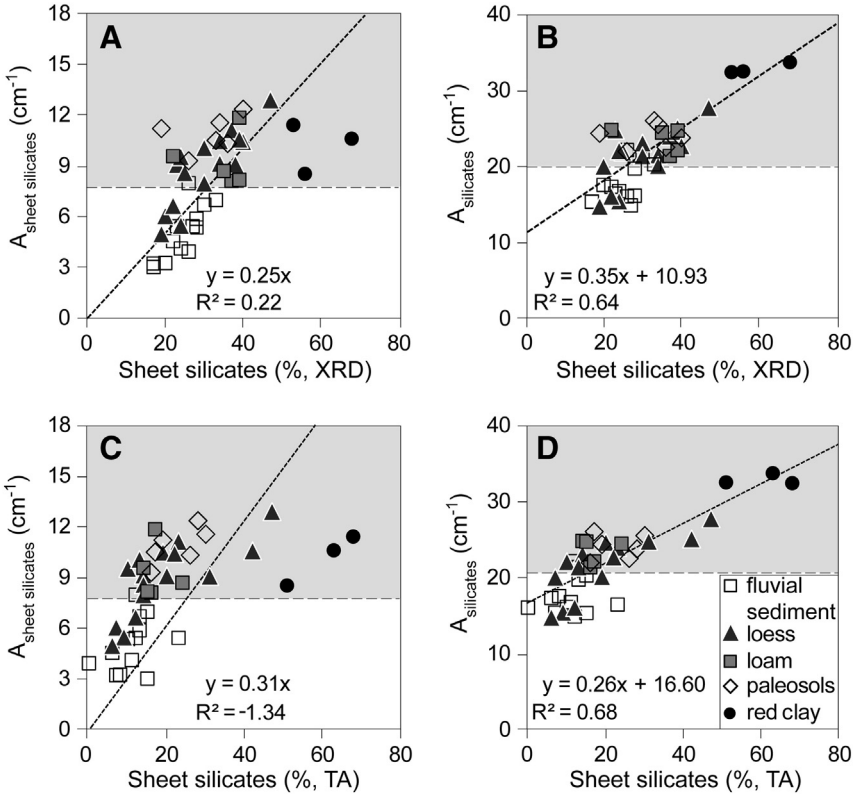

Fig. 4. Variation of characteristic infrared band areas ($A_{silicates}$ and $A_{sheet\ silicates}$) as a function of estimated abundances of sheet silicates by X-ray diffraction (A, B) and thermal analysis (C, D).

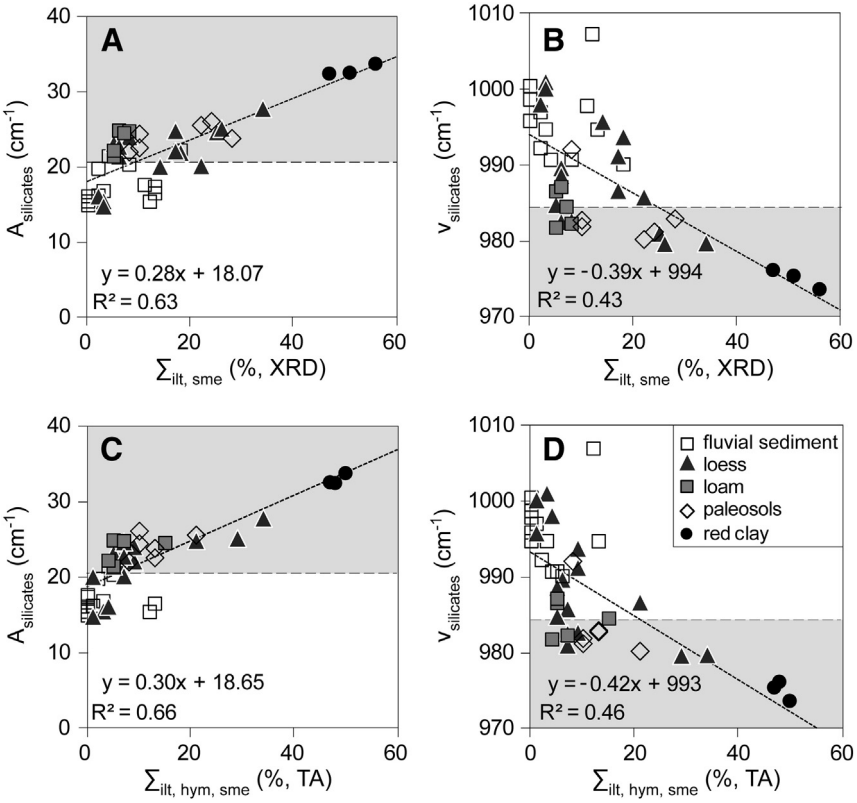

Fig. 5. The total amount of smectite and illite vs. infrared band areas typical for these minerals. Mineral percentages of the total amount of smectite and illite (and hydromuscovite) are obtained by X-ray diffraction (A, B) and thermal analysis (C, D).

The loss of molecular water between 47 and 268 °C by TA and the A_{water} values are positively correlated (Fig. 6C). Loess displays a wider field than the other sediment types and overlaps with loam and grey fluvial sediment. Again, the paleosol and red clay samples are clearly differ from the sediment types by showing both much higher molecular water content and A_{water} values. Therefore, the water content determined by ATR FTIR as A_{water} may provide a good estimate for the wetting capacity of sediments, which in turn can be applied as an indicator for clay rich zones more likely to suffer failures if conditions permit.

5.3. Effect of grain size and penetration depth of minerals (d_p) on the ATR FTIR spectra of sediments

Several correlations between infrared band areas and the amount of sheet silicates and carbonates by XRD and TA are identified along with several distinctive features for the different sediment types. However, further explanation may be warranted for the deviation of red clay samples from the main trendlines in the $A_{sheet\ silicates}$ and $A_{silicates}$ vs. sheet silicates plots (Fig. 4A–D). These samples usually occur below the trendline as their infrared band areas ($A_{sheet\ silicates}$, $A_{silicates}$) are lower than what would follow from the main trend lines. This means that the integrated absorbances of these particular spectral regions are smaller than what would follow from the amount of sheet silicates present in the sediments (smectite in particular).

The most likely explanation could be that clay minerals (especially smectite) usually show grain sizes akin to or smaller than the penetration depth of IR radiation in the considered spectral ranges (~2 and 0.5 μm at 1000 cm^{-1} and 3400 cm^{-1}, respectively; Table 2). The consequence is that if the grain size of a given mineral component is below the penetration depth specific to the particular mineral, then the absorbance of a component is underestimated. This is because the surface area of the mineral in contact with the ATR crystal is no longer proportional to its abundance in the sediment because the IR light

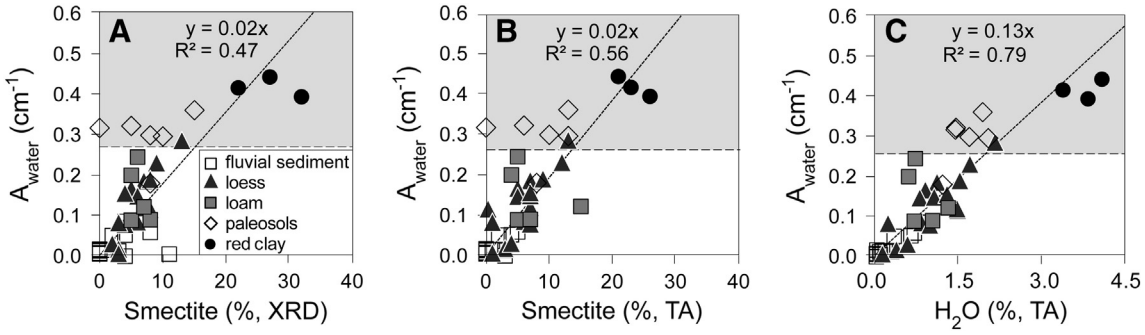

Fig. 6. Amounts of smectite (%) by X-ray diffraction (A) and thermal analysis (B) plotted as a function of infrared band area in the 1585-1725 cm^{-1} infrared region (A_{water}). C) The loss of molecular water by thermal analysis vs. the A_{water}.

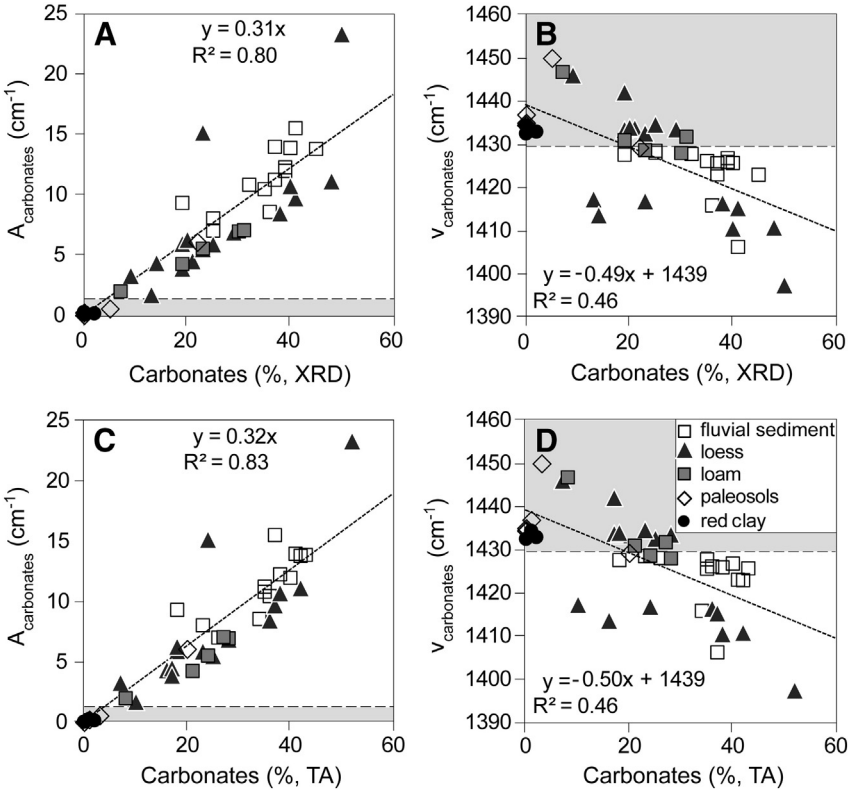

Fig. 7. Carbonates measured by X-ray diffraction (A, B) and thermal analysis (C, D) plotted against the integrated area and band maximum of carbonates ($A_{carbonates}$, $\nu_{carbonates}$).

(evanescent wave) could not fully sample the mineral to the maximum theoretical depth given by the penetration depth. Ideally, if the surface area in contact with the ATR crystal is constant, then the absorbance increases proportionally with the grain size up to the penetration depth. When the grain size is equal or larger than the penetration depth then the absorbance remains constant (given that the surface area in contact with the ATR crystal remains unchanged). This means that minerals with grain sizes below the penetration depth could show different absorbances depending on the grain size even if their surface area in contact with the ATR crystal is constant. It also follows that minerals with grain sizes larger than the depth of penetration (however not orders of magnitude larger) could be, in fact, effectively quantified since the absorbance in this case is thought to be only proportional to the surface area in contact with the ATR crystal. The surface area of a given mineral in contact with the ATR crystal is believed to be comparative to its proportion in the sediment. Thus ideally minerals with grain size larger than 2 μm could be better quantified because this is the thickness that is optimal for both the 'water' and 'Si-O' band region (Table 2).

Two important consequences include: (1) the minerals with an average grain size below 2 μm may only be quantified with high uncertainty, and (2) the low wave number bands at ~ 1000 cm^{-1} seem to be more sensitive to grain size effect than those at ~ 3400 cm^{-1}, which have smaller penetration depth (~0.5 as opposite to 2 for the bands at 1000 cm^{-1}).

Consequently, deviation from the main trends is expected for sediments with high concentration of clay minerals which are likely to have small grain sizes (Table 1, Supplementary Tables 3 and 4). This is particularly true for smectite which besides its low d_p also has small size (~0.1–1 μm, Yong et al., 2012). Individual particles of smectite have a larger contact area, although smaller penetration depth resulting in weaker ATR absorbance signals than what would follow from the surface area in contact with the ATR crystal. Indeed, it seems that the proportion of smectite correlates with the grain size fraction below

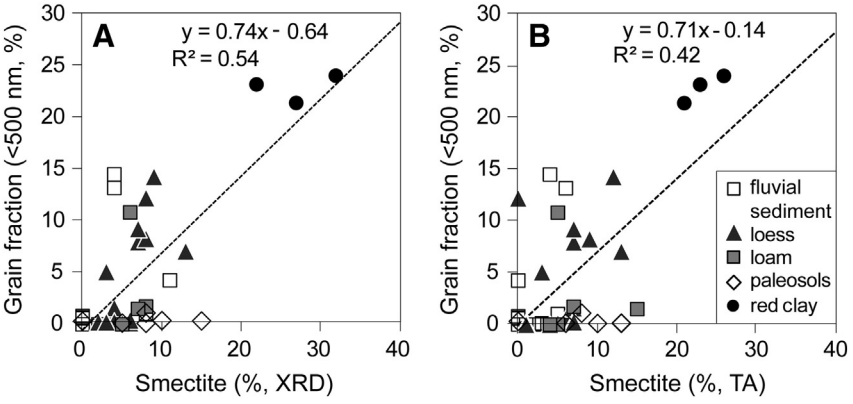

Fig. 8. Amounts of smectite (%) by X-ray diffraction (A) and thermal analysis (B) plotted as a function of the <500 nm particle fraction.

500 nm especially for red clay (Fig. 8A and B), which is the sediment that shows the most profound deviation from the main trends on absorbance vs. mineral proportion plots (Figs. 4, 5, 7).

There are also samples on the grain size fraction below 500 nm vs. smectite content plot with low proportion of smectite and high percentage of grain sizes below 500 nm (Table 1, Fig. 8A and B). These samples contain a higher fraction of amorphous material and even goethite occurs that may explain the higher contribution to this very fine grained fraction (Supplementary Table 3). Note that goethite in soils and sediments usually shows grain size below 0.1 μm (Langmuir, 1971). Nevertheless, there are also samples with higher percentages of smectite and lower proportion of 500 nm grains falling outside of the main trend. It is a possible consequence of different sample preparation by sieving and grinding, and the presence of aggregations arising from fine particles during particle analysis.

5.4. Contribution of clay minerals to the infrared features of the band at 825–1235 cm^{-1}

Correlation between $\Sigma_{ilt,\ sme}$ (by XRD and TA) vs. $A_{silicates}$ and $\nu_{silicates}$ from infrared spectra was also noticed which may imply the most significant relative contribution of smectite and illite to the infrared band area 825–1235 cm^{-1}. Infrared signals of quartz, feldspars, chlorite and muscovite also occur in the range of 825–1235 cm^{-1}, however, their estimated proportions do not seem to be correlated with $A_{silicates}$. This is because smectite and illite may usually have smaller average grain size and larger surface area than other sheet silicates (Yong et al., 2012). The contact with ATR crystal is closer for illite and smectite due to their fine platy particles which are not as rigid as that of quartz, feldspars, muscovite and chlorite. Consequently, the integrated area of the 'silicate region' (~1200–800 cm^{-1}) itself can provide a valuable indication, especially on the smectite and illite content of sediments.

5.5. Orientation of carbonates in powders

The ATR spectra of sediments with various carbonate contents reveal a significant shift (1398 to 1450 cm^{-1}) in the main band of carbonates at 1428 ± 11 cm^{-1} with the changing concentration of carbonates. The band position is shifted towards lower wave numbers with increasing carbonate content.

There are in principle two main reasons for band shifts in mineral ATR spectra. The first is that the presence of dolomite in the studied sediments also contributes to the enhanced scattering in the wave number and area of the band at 1428 cm^{-1}. Micro-scale changes in the mineral structure due to substitutions/incorporations of particular elements can also slightly shift the energy, therefore, the wave number of the particular absorption band. However, most bands other than that of carbonate show negligible shifts in wave numbers (Table 3). In addition, there is no indication by XRD and TA which would refer to significant variation in chemistry of the mineral constituents. While carbonates show the same degree of variation in proportions as sheet silicates, the shift in their prominent band at 1428 ± 11 cm^{-1} is much more significant (Table 3). The other explanation might be that the shift is due to the significant anisotropy and/or preferred orientation of carbonates as their modal proportion changes.

For this reason, we studied whether preferred orientation of calcite could be the reason for the observed band shift. First, a single oriented calcite crystal in three orthogonal directions (one being perpendicular to the c axis) was studied on the ATR plate. The IR spectrum of uniaxial crystals such as calcite shows a rather complicated behavior (Ketelaar and Haas, 1956). Fig. 9A shows three unpolarized average spectra of calcite representing one isotropic and two anisotropic sections (i.e., the average spectrum is the average of the two orthogonal and one diagonal spectra in each of the three sections). As light propagates along the c-axis of the calcite crystal, the infrared spectra remain unchanged during rotation. However, in the two other anisotropic sections the calcite crystal behaves strongly anisotropically and the spectra vary considerably during rotation. The average spectra in these two sections, nevertheless, are similar and only their absolute intensity differs (Fig. 9A).

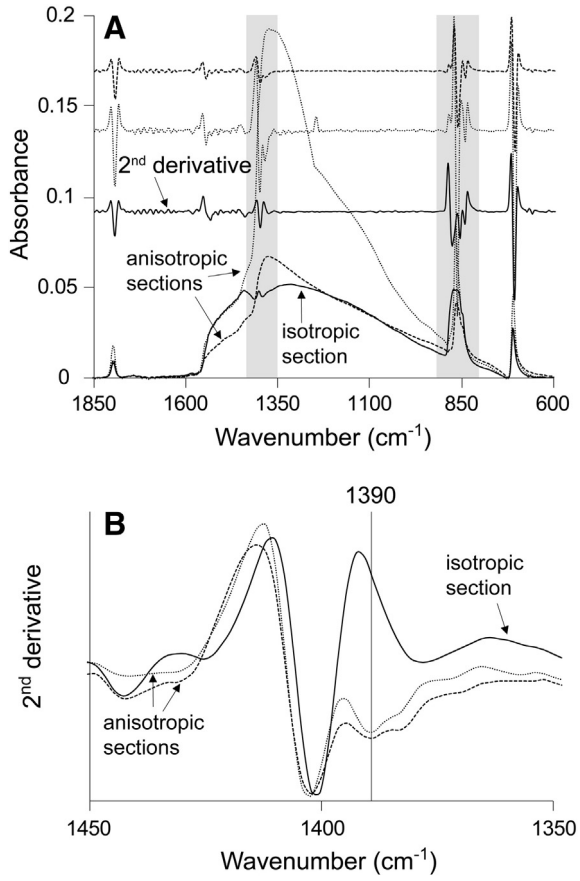

Fig. 9. Representative ATR FTIR spectra of the calcite cuboid from three orthogonal directions (A) and their second derivative curves in the 1350–1450 cm^{-1} wave number region (B). Each second derivative spectrum is stretched to illustrate the relative proportion of bands which contribute to the broad band in the region 1350–1450 cm^{-1}.

If we take a closer look at the second derivative curve, the similarity of the anisotropic sections are even more obvious (Fig. 9B). Not only the positions of the main bands at ~1390 cm^{-1} and 1400 cm^{-1}, but their relative changes are also similar. In contrast, the isotropic section seems to indicate positive amplitude of the secondary derivative spectrum at 1390 cm^{-1} and the direction of changes here appears to be opposite and more intense with respect to the anisotropic section. This suggests that in the isotropic section of calcite the main band appears at a slightly lower wave number. Therefore, it is very likely that the reason why the main band of carbonate shifts towards lower wave number is that the contribution of the isotropic sections becomes dominant. In other words, the c-axis of the calcite crystals is aligned perpendicular to the ATR plate. In fact, this makes perfect sense as probably this is how calcite crystals can minimize the effect of gentle pressure exerted by the ATR anvil.

Orientation effect was studied further in mechanical mixtures of kaolinite (KGa-1)–calcite (Beremend, Hungary) in different proportions (Fig. 10A and B). ATR spectra of binary mixtures show increasing shifts in wave numbers (from 1392 to 1433 cm^{-1}) with decreasing calcite content. This is in very good agreement what follows from our observations on the calcite cube.

In summary, the band shift towards lower wave numbers with increasing carbonate content is because that the c-axis is preferentially aligned perpendicular to the ATR plate due to the exerted pressure.

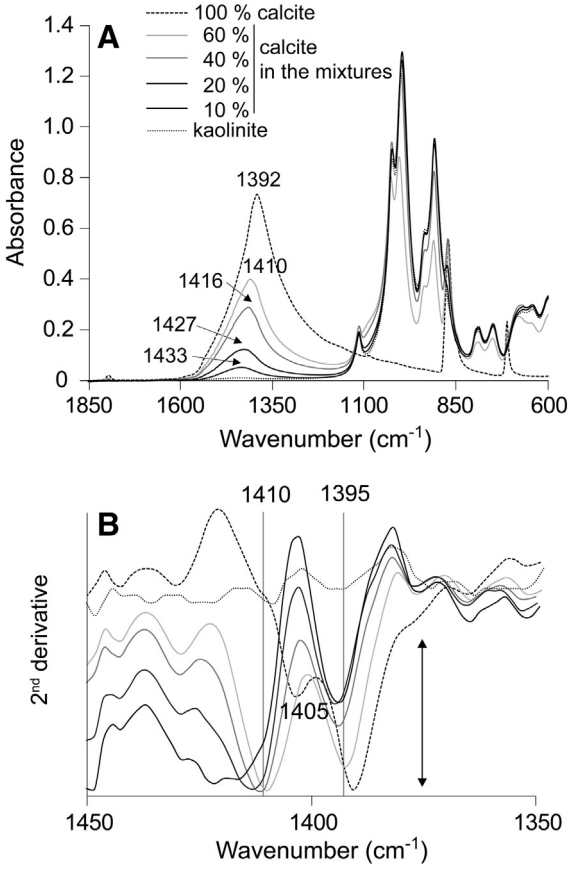

Fig. 10. ATR spectra of powdered calcite-kaolinite mixture (A) and their second derivative curves in the 1350–1450 cm^{-1} wave number region (B). Each second derivative spectrum is stretched to illustrate the relative proportion of bands those contribute the broad band in the region 1350–1450 cm^{-1}.

5.6. Kaolinite in ATR spectra of sediments and its importance

As weathering proceeds, formation of smectites and leaching of carbonates will create weakness zones more susceptible to sliding. In addition, the low permeability and high water absorbing capacity of smectites hinders water flow and the stagnating underground water may further intensify weathering. This also makes pre-existing smectite-rich zones more slippery.

The occurrence of sheet silicates, especially kaolinite seems to be common in landslide-prone sediments and its amount is considered to play an important role in sliding (i.e., Wen and Chen, 2007; Summa et al., 2010). Kaolinite is also known to occur in larger modal abundance with the increasing degree of weathering (Singer, 1984). This means that in potential sliding zones the concentration of sheet silicates (especially smectite and kaolinite) and carbonates are thought to increase and decrease, respectively. As was shown, particular infrared parameters ($A_{silicates}$ and A_{water}) correlate reasonably well with smectite content, whereas $A_{carbonates}$ is proportional to the carbonate content determined by XRD and TA. Similar relations for kaolinite were not identified due to the difficulties during its XRD (i.e., overlap with chlorite band) and TA quantifications (i.e., high temperature exothermic peak and overlap with carbonate and muscovite bands). XRD and TA results show that a large number of samples contain relatively high concentration of chlorite (average 10%) and traces of kaolinite also occur in some samples. The presence of kaolinite, however, was confirmed in each sample by ATR FTIR analysis. The overlapping makes it difficult to distinguish and quantify between kaolinite and chlorite by XRD technique when both are present in a clay mineral assemblage (Guo and Underwood, 2011). Therefore, the information about the amount and mineralogy of kaolinite derived from infrared spectroscopy may differ to that of XRD (and TA). It seems plausible, however, that even trace amount of kaolinite can be determined and estimated using the presence and the area of one of its prominent absorption band at 3697 cm^{-1}.

As we have demonstrated, the silicate/carbonate ratios are expected to be significantly higher in more weathered zones, which are more likely to accommodate sliding. Accordingly, kaolinite is also more abundant in these zones, thus, if $A_{water}/A_{carbonates}$ and $A_{silicates}/A_{carbonates}$ ratios are plotted against $A_{kaolinite}$, sheet silicate rich and carbonate poor sediments would fall in different parts of the diagram (Fig. 11A and B). The band ratios were visualized on a logarithmic scale and carbonate poor and sheet silicate rich sediments fall in the upper right part of the diagram. Both paleosol and red clay have distinctive higher values of $A_{water}/A_{carbonates}$ (average 3.65, min. 0.03–max. 8.02), $A_{silicates}/A_{carbonates}$ (315.30, 41.95–622.24) and $A_{kaolinite}$ (0.09, 0.07–0.15) than in loess, loam and grey fluvial sediment. Only one paleosol sample (K2-6) has higher carbonate content than other paleosols, therefore overlaps with other observed sediments. Grey fluvial sediment and loam form different clusters but overlap with loess.

6. Conclusions

The results of this study demonstrate that on the bulk powder of a representative collection of sediments (grey fluvial sediment, loess, paleosols, intercalated loam samples between sand–sandstone and red clay) from a landslide area that using infrared band areas of carbonates and sheet silicates show good agreement with classic XRD and TA methods. Therefore, ATR FTIR methods could be applied complementary to classic TA and XRD methods in classifying natural sediments, if a quick and cost effective analysis is needed. This methodology can be

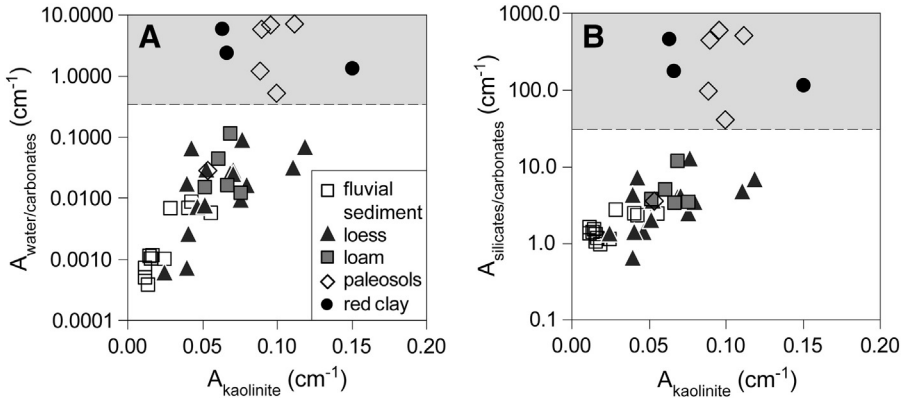

Fig. 11. Variation of the ratio of infrared band areas ($A_{water}/A_{carbonates}$ (A) and $A_{silicates}/A_{carbonates}$ (B)) with $A_{kaolinite}$.

directly applied for the identification of weakness zones in landslides. Kaolinite infrared band area vs. silicates/carbonate and water/carbonate infrared band areas were found to be especially useful for the identification of paleosols and red clay. These latter two sediment types or clay-rich and carbonate poor sediments, in general, are expected to occur in elevated quantities along sliding zones or facilitate the onset of sliding.

The ATR spectra of sediments showed that grain size, penetration depth and orientation effects can contribute to changes in magnitude and wave number shift of characteristic infrared bands. The large sample set including various modal abundances of common minerals in sediments ensures the feasibility of the developed ATR FTIR methodology.

Acknowledgements

The authors would like to thank József Vatai, László Koloszár, Csaba Jerabek, Géza Kutasi (Geological and Geophysical Institute of Hungary) for their help in the site investigation and borehole sampling, Katalin Fehér (Department of Environmental and Landscape Geography, Eötvös Loránd University) for her suggestions in sample preparation to laser particle analysis by Horiba Partica LA-950 V2 (Eötvös Loránd University Faculty of Science Research and Instrument Core Facility – ELTE FS-RICF), Csaba Németh (Research Centre for Natural Sciences) for his help in ATR FTIR measurement, and Gábor Koller for help with calcite procurement. The authors are also thankful for the constructive comments from two anonymous reviewers and the careful editorial handling of J. Knight. This work was supported by the Bolyai Postdoctoral Fellowship Program, a Marie Curie International Reintegration Grant (NAMS-230937) and a postdoctoral grant (PD101683) of the Hungarian Scientific Research Found to I. Kovács. This research was made in agreement between ELTE and MFGI (TTK 2461/1/2013 and MFGI 206-114/2013).

Appendix A. Supplementary data

Supplementary data to this article can be found online at http://dx.doi.org/10.1016/j.sedgeo.2014.08.005.

References

Adamu, M.B., 2010. Fourier transform infrared spectroscopic determination of shale minerals in reservoir rocks. Nigerian Journal of Basic and Applied Science 18, 6–18.
Azañón, J.M., Azor, A., Yesares, J., Tsige, M., Mateos, R.M., Nieto, F., Delgado, J., López-Chicano, M., Martín, W., Rodríguez-Fernández, J., 2010. Regional-scale high-plasticity clay-bearing formation as controlling factor on landslides in Southeast Spain. Geomorphology 120, 26–37.
Bertaux, J., Fröhlic, F., Ildefonse, P., 1998. Multicomponent analysis of FTIR spectra; quantification of amorphous and crystallized mineral phases in synthetic and natural sediments. Journal of Sedimentary Research 68, 440–447.
Besson, G., Drits, V.A., 1997. Refined relationships between chemical composition of dioctahedral fine-grained micaceous minerals and their infrared spectra within the OH stretching region. Part I: Identification of the OH stretching bands. Clays and Clay Minerals 45, 170–183.
Breen, C., Clegg, F., Herron, M.M., Hild, G.P., Hillier, S., Hughes, T.L., Jones, T.G.J., Matteson, A., Yarwood, J., 2008. Bulk mineralogical characterisation of oilfield reservoir rocks and sandstones using Diffuse Reflectance Infrared Fourier Transform Spectroscopy and Partial Least Squares analysis. Journal of Petroleum Science and Engineering 60, 1–17.
Chemtob, S.M., Glotch, T.D., Rossman, G.R., 2010. ATR-IR Spectroscopy for in situ mineral analysis on planetary surfaces: steps toward a forward model. Proceedings of the Lunar and Planetary Science Conference, LPI, Houston, Texas 2198, pp. 1–2.
Dent, G., 1996. Preparation of Samples for IR spectroscopy as KBr disks. Internet Journal of Vibrational Spectroscopy 1, 1–2.
Eshel, G., Levy, G.J., Mingelgrin, U., Singer, M.J., 2004. Critical evaluation of the use of laser diffraction for particle-size distribution analysis. Soil Science Society of America Journal 68, 736–743.
Essington, M.E., 2004. Chemical weathering. In: Essington, M.E. (Ed.), Soil and water chemistry: An integrative approach. CRC Press, Boca Raton, pp. 101–128.
Farkas, J., 2011. Szakértői vélemény Kulcs felszínmozgásos területeinek vizsgálatáról. Farkas Geotechnikai Szakértői és Laboratóriumi Ltd., Budapest (166 pp. Expert evidence about landslide prone areas of Kulcs, in Hungarian).
Farmer, V.C., 1974. The infrared spectra of minerals. Mineralogical Society, London.
Földvári, M., 2011. Handbook of thermogravimetric system of minerals and its use in geological practice. Occasional Papers of the Geological Institute of Hungary 213 (179 pp.).
Földvári, M., Kovács-Pálffy, P., 2002. Mineralogical study of the Tengelic Formation and the loess complex of the Tolna Hegyhát and Mórágy Hills areas (Hungary). Acta Geologica Hungarica 45, 247–263.
Glotch, T.D., Chemtob, S.M., Rossman, G.R., 2007. Attenuated total reflection as an in situ infrared spectroscopic method for mineral identification. Proceedings of the Lunar and Planetary Science Conference, LPI, Houston, Texas 1731, pp. 1–2.
Guiliano, M., Asia, L., Onoratini, G., Mille, G., 2007. Applications of diamond crystal ATR FTIR spectroscopy to the characterization of ambers. Spectrochimica Acta Part A 67, 1407–1411.
Guo, J., Underwood, M.B., 2011. Data report: refined method for calculating percentages of kaolinite and chlorite from X-ray diffraction data, with application to the Nankai margin of southwest Japan. In: Kinoshita, M., Tobin, H., Ashi, J., Kimura, G., Lallemant, S., Screaton, E.J., Curewitz, D., Masago, H., Moe, K.T. (Eds.), Proceedings of the Integrated Ocean Drilling Program 314/315/316. Integrated Ocean Drilling Program Management International Inc., Washington, DC, pp. 1–14.
Herbert, T.D., Tom, B.A., Burnett, C., 1992. Precise major components determinations in deep sea sediments using Fourier transform infrared spectroscopy. Geochimica et Cosmochimica Acta 56, 1759–1763.
Hillier, S., Fraser, A., Wood, K., 2000. Use of full pattern fitting of infrared spectra to determine the composition of river suspended sediment. Annual meeting of the Clay Minerals Society, Loyola University, Chicago, p. (62 pp.).
Hlavay, J., Jonas, K., Elek, S., Inczedy, J., 1978. Characterization of the particle size and the crystallinity of certain minerals by IR spectrophotometry and other instrumental methods-II. Investigations on quartz and feldspar. Clays and Clay Minerals 26, 139–143.
Horiba, 2008. AN157 applications note. Refractive index selection for powder mixtures. Horiba Instruments Inc., pp. 1–5.
Hughes, T.L., Methven, C.M., Jones, T.G.J., Pelham, S.E., Fletcher, P., Hall, C., 1995. Determining cement composition by Fourier transform infrared spectroscopy. Advanced Cement Based Materials 2, 91–104.
Jian, W., Wang, Z., Yin, K., 2009. Mechanism of the Anlesi landslide in the Three Gorges Reservoir, China. Engineering Geology 108, 86–95.
Johnston, C.T., Premachandra, G.S., 2001. Polarized ATR-FTIR study of smectite in aqueous suspension. Langmuir 17, 3712–3718.
Jonasz, M., 1991. Size, shape, composition and structure of microparticles from light scattering. In: Syvitski, J.P.M. (Ed.), Principles, methods, and application of particle size analysis. Cambridge University Press, Cambridge, pp. 143–162.
Jung, H.-J., Malek, M.A., Ryu, J., Kim, B., Song, J.-C., Kim, H., Ro, C.-U., 2010. Speciation of individual mineral particles of micrometer size by the combined use of attenuated total reflectance-Fourier transform-infrared imaging and quantitative energy-dispersive electron probe x-ray microanalysis techniques. Analytical Chemistry 82, 6193–6202.
Ketelaar, J.A.A., Haas, C., 1956. Infrared emission spectrum of calcite. Physica 22, 1283–1285.
Kodama, H., Oinuma, K., 1962. Identification of kaolin minerals in the presence of chlorite by X-ray diffraction and infrared absorption spectra. Clays and Clay Minerals 11, 236–249.
Kovács, I.J., Hermann, J., O'Neill, H.St.C., Fitzgerald, J., Sambridge, M., Horváth, G., 2008. Quantitative IR spectroscopy with unpolarized light Part II: Empirical evidence and practical application. American Mineralogist 93, 765–778.
Kumar, R.S., Rajkumar, P., 2013. Characterization of minerals in air dust particles in the state of Tamilnadu, India through FTIR spectroscopy. Atmospheric Chemistry and Physics Discussions 13, 22221–22248.
Langmuir, D., 1971. Particle size effect on the reaction goethite = hematite + water. American Journal of Science 271, 147–156.
Libowitzky, E., Rossman, G.R., 1996. Principles of quantitative absorbance measurements in anisotropic crystals. Physics and Chemistry of Minerals 23, 319–327.
Libowitzky, E., Rossman, G.R., 1997. An IR absorption calibration for water in minerals. American Mineralogist 82, 1111–1115.
Lide, D.R., 2005. Physical and optical properties of minerals. In: Lide, D.R. (Ed.), CRC handbook of chemistry and physics (86th). CRC Press, Boca Raton, FL, pp. 151–157.
Madejová, J., 2003. FTIR techniques in clay mineral studies. Vibrational Spectroscopy 31, 1–10.
Madejová, J., Komadel, P., 2001. Baseline studies of the Clay Minerals Society source clays: infrared methods. Clays and Clay Minerals 49, 410–432.
Ozer, M., Orhan, M., Isik, N.S., 2010. Effect of particle optical properties on size distribution of soils obtained by laser diffraction. Environmental and Engineering Geoscience 16, 163–173.
Palayangoda, S.S., Nguyen, Q.P., 2012. An ATR-FTIR procedure for quantitative analysis of mineral constituents and kerogen in oil shale. Oil Shale 29, 344–356.
Paulik, J., Paulik, F., 1981. Simultaneous thermoanalytical examinations by means of the DerivatographWilson and Wilson's Comprehensive Analytical Chemistry 12. Elsevier, Amsterdam (277 pp.).
Pécsi, M., Schweitzer, F., 1993. Long-term terrestrial records of the Middle Danubian Basin. Quaternary International 17, 5–14.
Planinsek, O., Planinsek, D., Zega, A., Breznik, M., Srčič, S., 2006. Surface analysis of powder binary mixtures with ATR FTIR spectroscopy. International Journal of Pharmaceutics 319, 13–19.
Reig, F.B., Adelantado, J.V.G., Moya Moreno, M.C.M., 2002. FTIR quantitative analysis of calcium carbonate (calcite) and silica (quartz) mixtures using the constant ratio method. Application to geological samples. Talanta 58, 811–821.
Rónai, A., Bartha, F., Krolopp, E., 1965. A kulcsi löszfeltárás szelvénye. Research Report of the Hungarian Geological Institute in 1963, Budapest, pp. 167–185 (Geological profile of the loess at Kulcs, in Hungarian).

Sajó, I., 1994. Powder diffraction phase analytical system 1.7, users guide. Aluterv-FKI Ltd., Budapest, pp. 1–81.
Sambridge, M., Gerald, J.F., Kovács, I.J., O'Neill, H.St.C., Hermann, J., 2008. Quantitative absorbance spectroscopy with unpolarized light: Part I. Physical and mathematical development. American Mineralogist 93, 751–764.
Schroeder, P.A., 2002. Infrared spectroscopy in clay science. In: Guggenheim, S., Rule, A. (Eds.), Teaching clay science. Clay Minerals Society Workshop Series, Aurora 13, pp. 181–202.
Singer, A., 1984. The paleoclimatic interpretation of clay minerals in sediments – a review. Earth Science Reviews 21, 251–293.
Środoń, J., Drits, V.A., Mccarty, D.K., Hsieh, J.C.C., Eberl, D.D., 2001. Quantitative XRD analysis of clay-rich rocks from random preparations. Clays and Clay Minerals 49, 514–528.
Summa, V., Tateo, F., Gianossi, M.L., Bonelli, C.G., 2010. Influence of clay mineralogy on the stability of a landslide in Plio-Pleistocene clay sediments near Grassano (Southern Italy). Catena 80, 75–85.
Szalai, S., Konkolyné, B.Z., Lakatos, M., Szentimrey, T., 2005. Some characteristics of the climate of Hungary since 1901. Hungarian Meteorological Service, Budapest, pp. 1–12.
Tóth, J., Udvardi, B., Kovács, I.J., Falus, Gy, Szabó, Cs, Troskot-Čorbić, T., Slavković, R., 2012. Analytical development in FTIR analysis of clay minerals. MOL Scientific Magazine 1, pp. 52–61.
Udvardi, B., Kovács, I., Szabó, Cs, Mihály, J., Németh, Cs, 2012. Aggregation of kaolinites and swelling-drying effect in microaggregates of bentonites. Environmental Scientific Conference of the Carpathian Basin, Veszprém, Hungary, pp. 140–145.
Urbaniak-Domagala, W., 2012. The use of the spectrometric technique FTIR-ATR to examine the polymers surface. In: Farrukh, M.A. (Ed.), Advanced aspects of spectroscopy. InTech, Croatia, pp. 85–104.
Vaculícová, L., Plevová, E., 2005. Identification of clay minerals and micas in sedimentary rocks. Acta Geodynamica et Geomaterialia 2, 167–175.
Van der Marel, H.W., Beutelspacher, H., 1976. Atlas of infrared spectroscopy of clay minerals and their admixtures. Elsevier Scientific Publishing Company, Amsterdam (396 pp.).
Varga, A., Újvári, G., Raucsik, B., 2011. Tectonic versus climatic control on the evolution of a loess-paleosol sequence at Beremend, Hungary: An integrated approach based on paleoecological, clay mineralogical and geochemical data. Quaternary International 240, 71–86.
Wada, K., 1967. A study of hydroxyl groups in kaolin minerals utilizing selective deuteration and infrared spectroscopy. Clay Minerals 7, 51–61.
Wang, H.B., Zhou, B., Wu, S.R., Shi, J.S., Li, B., 2011. Characteristic analysis of large-scale loess landslides: a case study in Baoji City of Loess Plateau of Northwest China. Natural Hazards and Earth System Sciences 11, 1829–1837.
Washburn, K.E., Birdwell, J.E., 2013. Multivariate analysis of ATR-FTIR spectra for assessment of oil shale organic geochemical properties. Organic Geochemistry 63, 1–7.
Wen, B.P., Chen, H.Y., 2007. Mineral compositions and elements concentrations as indicators for the role of groundwater in the development of landslide slip zones: a case Study of large-scale landslides in the Three Gorges Area in China. Earth Science Frontiers 14, 98–106.
Yong, R.N., Nakamo, M., Pusch, R., 2012. Swelling clays. In: Yong, R.N., Nakano, M., Pusch, R. (Eds.), Environmental soil properties and behavior. CRC Press, Boca Canton, pp. 133–162.